Silica-coated gold nanorods biofunctionalization for localized surface plasmon resonance (LSPR) biosensing

Vincent Pellas, Fadoua Sallem, Juliette Blanchard, Antoine Miche, Sara Martinez Concheso, Christophe Méthivier, Michèle Salmain, Souhir Boujday

Silica-coated gold nanorods biofunctionalization for localized surface plasmon resonance (LSPR) biosensing

Vincent Pellas,[a,b] Fadoua Sallem,[a] Juliette Blanchard,[a] Antoine Miche,[a] Sara Martinez Concheso,[a] Christophe Méthivier,[a] Michèle Salmain[b,*], Souhir Boujday[a,*]

[a] Sorbonne Université, CNRS, Laboratoire de Réactivité de Surface (LRS), F-75005 Paris, France

[b] Sorbonne Université, CNRS, Institut Parisien de Chimie Moléculaire (IPCM), F-75005 Paris

Abstract

We introduce here the engineering of nanobiosensors designed from gold nanorods coated with an ultrathin layer of silica (AuNR@SiO_2) and biofunctionalized with antibodies for the Localized Surface Plasmon Resonance (LSPR) biosensing of proteins. Despite the outstanding properties of AuNRs, their use for LSPR biosensing is limited due to the presence of the surfactant cetyltrimethylammonium bromide (CTAB) – mandatory for their synthesis - which forms a strongly-bounded and positively-charged bilayer at their surface and significantly complicates their bio-functionalization. When coated with a thin layer of silica, these nanomaterials exhibit an improved sensitivity to refractive index change which augurs for better analytical performances. Here, we undertook an in-depth investigation of the biofunctionalization of AuNR@SiO_2 *via* three different routes to design and test a label-free LSPR biosensor operating in solution. In the first route, we took advantage of the negatively charged external silica shell to immobilize anti-rabbit IgG antibody by electrostatic physisorption. In the second and third routes, the silica surface was reacted with thiol or aldehyde terminated silanes, subsequently utilized to covalently attach anti-rabbit IgG antibody to the surface. The resulting nanoprobes were characterized by a wide range of physical methods (TEM, XPS, DLS, ELS and UV-Visible spectroscopy) then tested for the biosensing of rabbit-IgG. The three nanobiosensors maintain an excellent colloidal stability after analyte recognition and exhibit extremely high analytical performances in terms of specificity and dynamic range, with an LoD down to 12 ng/mL.

Keywords

Gold Nanorods, Silica Coating, Surface Chemistry, Core−Shell, LSPR, Immunosensing

1. Introduction

Refractometric biosensors are analytical devices tightly associating a bioreceptor and an optical transducer whose response arises from the change of refractive index that occurs upon binding of the target to the bioreceptor at the solid/ liquid interface. Aside from the highly popular label-free surface plasmon resonance biosensors, localized surface plasmon resonance (LSPR) biosensors are gaining increasing interest because (1) they are cheaper label-free transducers, (2) they enable real time sensing, (3) they require less technically demanding instrumentation as compared to SPR and finally (4) they are easy to miniaturize [1–3].

The LSPR phenomenon results from the interaction of light with metal nanostructures (typically coinage metal nanoparticles) that gives rise to characteristic extinction whose position depends on the nanostructure but typically ranges from the near-UV to the near-infrared spectra range. The principle of LSPR-based biosensors relies on the shift of the LSPR band position of plasmonic nanostructures that happens when the refractive index (RI) of the surrounding medium changes. The change of local refractive index typically occurs when an antigen binds to antibody-coated gold nanoparticles that translates into a red shift of the plasmon band. Plasmonic nanostructures are characterized by the RI sensitivity factor that is strongly dependent on their size, shape and composition [4]. Furthermore, the shift of the plasmon band position with respect to RI change is highly distance-dependent [5] and comparatively to SPR, the probing distance of LSPR is much shorter, that is comparable to biomacromolecules size, meaning that the bioreceptor – target complexes occupy the entirety of the evanescent field [6].

Among the variety of plasmonic nanoparticles synthetically accessible by bottom-up methods, gold nanorods (AuNR) are particularly well suited to design LSPR nanobiosensors [7]. Besides the transverse plasmon band (t-LSPR) at ca. 520 nm, AuNR manifest a second extinction peak at higher wavelength known as the longitudinal plasmon band (l-LSPR) [8]. The position of this band can be tuned from the visible to the near-IR spectral range according to the AuNR aspect ratio, i.e. the length divided by the width [9]. Most importantly, the longitudinal band of AuNR generally displays a high RI sensitivity [10,11]. For instance, AuNR-coated glass chips exhibit a bulk RI sensitivity of 252 nm/RIU (Refractive Index Unit) that is 4 times that of nanospheres [12]. Consequently, binding events may be more sensitively detected with AuNR-based LSPR biosensors.

Few examples of AuNR-based LSPR biosensors operating in the solid phase with nanostructured flat substrates [13] or in solution [14–17] have been reported to date. Moreover, the latter ones were mostly based on nanoparticle aggregation upon target binding, resulting in a large decrease of the LSPR band intensity. This limitation in the use of AuNRs for biosensing, despite their outstanding properties, is caused by the presence of the surfactant cetyltrimethylammonium bromide (CTAB) – mandatory for their synthesis - which forms a strongly-bounded and positively-charged bilayer at their surface and significantly complicates their functionalization. In addition, CTAB can also induce non-specific binding of molecules via electrostatic interactions [11]. Grafting of PEG has been proposed to functionalize AuNR with bioligands [18]. Alternatively, coating of AuNR with a shell of silica screens the CTAB bilayer and enables further biofunctionalization via organosilane chemistry [19]. Furthermore, mesoporous silica-coated AuNR (AuNR@SiO_2) maintain a high sensitivity to RI change [20]. We, and others, have proved that the sensitivity factor could even be enhanced for

AuNR@SiO_2 with respect to CTAB-coated AuNR, provided the silica shell thickness is thin enough (2 – 4 nm) [21,22]. Nevertheless, very few examples of AuNR@SiO_2-based LSPR biosensors have been reported in the literature as their surface chemistry is still to be mastered [21,23].

We have recently introduced homogeneous, solution-phase LSPR biosensors based on colloidal gold and core-shell Au@Ag nanospheres conjugated to an antibody for the detection of a bacterial toxin target [24,25]. We have also designed an efficient and reproducible procedure to cover AuNR with a ultrathin layer of silica and found that their RI sensitivity factor was enhanced by 30 % compared to CTAB-coated AuNR, which let us anticipate better analytical performances [22]. More generally, silica surface functionalization is easily amenable via silane condensation on silanol groups [26,27].

Herein we report the biofunctionalization of AuNR@SiO_2 via three different routes to design and test a label-free LSPR immunosensor of rabbit IgG operating in solution. This target is a convenient model to set up biosensors, enabling our own nanoprobe performances to be compared with the early designed nanoprobe reported by Ma et al. for the detection of human IgG [16]. In the first route, we took advantage of the negatively charged external silica shell to immobilize anti-rabbit IgG antibody by electrostatic physisorption. In the second and third route, the silica surface was reacted with thiol or aldehyde terminated silane, subsequently utilized to covalently attach anti-rabbit IgG antibody to the surface. The different steps of surface modification were deeply characterized and the biofunctionalization investigated in terms of both kinetics and thermodynamics. Finally, the resulting nanoprobes were applied to the detection of the rabbit IgG analyte and their analytical performances assessed and comparatively discussed.

2. Materials and methods

2.1. Chemicals and Reagents

Tetraethyl orthosilicate (≥99.0%, TEOS), cetyltrimethylammonium bromide (BioUltra ≥99.0%, CTAB), (3-mercaptopropyl)trimethoxysilane (≥95%, MPTMS), 5,5′-dithiobis(2-nitrobenzoic acid) (≥98%; DTNB), tris(2-carboxyethyl) phosphine hydrochloride (≥ 98%, TCEP), m-maleimidobenzoyl-N-hydroxysulfosuccinimide ester (≥ 80%, Sulfo-MBS), sodium cyanoborohydride (≥ 95%), fluorescein 5-isothiocyanate (≥ 90% isomer I, FITC), ammonium chloride (≥95.5%), bovine serum albumin (≥98%, BSA), rabbit IgG (≥95%), sodium dihydrogen phosphate (≥99.0%), and anhydrous disodium hydrogen phosphate (>99.0%) were purchased from Sigma-Aldrich. Hydrochloric acid (37%; HCl) was purchased from VWR chemicals. 3-Triethoxysilylbutyraldehyde (≥90%, TEBA) was purchased from Gelest. Glycerol (99.5%), sodium carbonate (≥99.8%), and sodium hydrogen carbonate (≥99.5%) were purchased from Humeau. Affinity-purified polyclonal goat anti-rabbit IgG (anti-rIgG) was purchased from Jackson Immunoresearch. All aqueous solutions were prepared with Millipore ultrapure water (18.2 MΩ.cm^{-1}).

2.2. Characterization techniques

UV-Vis Spectroscopy. UV-Visible (UV-Vis) extinction spectra were recorded on a Cary 50

spectrophotometer (Varian, Inc.) and the analysis of colloidal dispersions was performed in the 400–1100 nm range using 1-cm optical pathlength plastic cuvettes. According to refs. [28,29], Abs_{400} linearly correlates with the Au^0 concentration and Abs_{400} = 1.2 at 400 nm corresponds to 100 % reduction of a 0.5 mM gold salt solution. According to this relation, the reduction yield of Au^{3+} was estimated. Mathematical determination of λ_{max} was done from the first order derivative spectra as recommended in refs [30,31].

Dynamic light scattering (DLS) and electrophoretic light scattering (ELS). DLS and ELS measurements were performed using a Litesizer™ 500 apparatus (Anton Paar) equipped with a 658 nm laser operating at 40 mW. The scattered light collection angle was set to 90°. The zeta potential was measured in a Ω- shaped capillary tube cuvette with an applied potential of 150V. Gold nanorods being anisotropic particles, their diffusion is associated to two characteristic times that correspond to two motions: rotational and translational. These two times lead to two signals in the particle size distribution, one of low intensity, at relatively low dimensions (ca. 10 nm equivalent hydrodynamic diameter) and associate to rotational diffusion, and the other, more intense, at larger dimensions (ca. 100 nm equivalent hydrodynamic diameter), associated to translational diffusion [32].

Transmission electron microscopy (TEM). TEM images of AuNR and AuNR@SiO_2 were obtained using a JEOL JEM 1011 transmission electron microscope (TEM) operating at an accelerating voltage of 100 kV. Samples were prepared by depositing a drop of water-diluted (x20) particle suspension onto a carbon-coated copper grid and drying the grid at room temperature before imaging. Size distribution of AuNR and silica shell thickness of AuNR@SiO_2 were established by counting a minimum of 200 particles and 200 shells using Image J software.

X-ray photoelectron spectroscopy (XPS). XPS analyses were performed using a Scienta Omicron Argus X-ray photoelectron spectrometer equipped with Al Kα monochromatic radiation source (1486.6 eV) and operating at 280 W power. Analysis was performed under an ultrahigh vacuum ($<10^{-9}$ mbar). The photoelectrons were analyzed in a direction making an angle of 45° to the surface. Spectra were recorded at a passing energy of 100 eV for the survey spectrum and 20 eV for the S_{2p} region. Data analysis was carried out using Casa XPS v.2.3.15 software (Casa Software Ltd., U.K.). Colloidal suspensions (1.5 mL) were concentrated by centrifugation (10 min at 9000 rpm) to 30 µL. The resulting suspensions were deposited as 10µL drops on indium substrates and dried in air for 2 h before analysis.

2.3. Surface functionalization of core-shell gold-silica nanorods

Synthesis of gold nanorods (AuNR) and core-shell gold nanorods-silica (AuNR@SiO_2)

AuNR were synthesized and characterized by TEM, UV-Vis spectroscopy, DLS and ELS following the protocol detailed in a previous work [22]. The size of the synthesized AuNR is L= 102 (± 7) nm, l= 40 (± 2) nm with aspect ratio (AR) of 2.58 (± 0.2) and λ_{max} = 716 nm. A 3-nm silica layer was grown on gold nanorods as previously described [22]. Briefly, prior to SiO_2 coating, the AuNRs suspension was diluted with water to adjust the Au^0 and CTAB concentrations to 1.6 and ca. 6 mM, respectively (CTAB concentration value is estimated based on the dilution of the fraction of growth solution remaining with the AuNRs after

centrifugation). The initial pH was adjusted to 4.0 by adding HCl or NaOH solution (0.1 M) and kept under stirring for 20 min at 400 rpm. Then, 41 µL of MPTMS acting as primer (100 mM) in EtOH were added under stirring (400 rpm) for 3 h. Next, 62 µL of TEOS in MeOH (20%) was added for a final Au/TEOS mole ratio of 1:1.80, and the suspension was stirred for 1 h at 800 rpm. The pH was adjusted to 8.0 using 0.1 M NaOH and the suspension was stirred for 20 min at 400 rpm before being kept without stirring for 20 h at room temperature. The resulting core-shell particles, referred to AuNR@SiO_2, were sonicated and centrifuged at 7060 rcf for 15 min. The sedimented particles were washed four times with EtOH and twice with water and finally redispersed in 5 mL of water.

Silanes assembly on AuNR@SiO_2

AuNR@SiO_2 suspension (3.0 mL; surface area: $8.11x10^{15}$ nm^2, [AuNR@SiO_2] = 15.7 nM, OD_{max} ~ 6.0) in EtOH: H_2O (95:5 v/v) was sonicated for 5 min and then heated at 60°C under stirring for 20 min in the oven in order to homogenize the solution. Then, 1.25 µL of pure MPTMS (or 1.64 µL of TEBA) (corresponding to 100 eq/surface OH; 2.24 mM final) was added to the solution, which was stirred for 17 h at 60°C and 500 rpm. Particles were washed twice with ethanol and twice with Milli Q water by centrifugation (15 min, 9000 rpm) and stored in 3.0 mL of Milli Q water.

Quantification of thiol functions on AuNR@SiO_2-MPTMS

Quantification of thiol groups in AuNR@SiO_2-MPTMS was carried out by Ellman's reagent (DTNB) assay in triplicate [33]. AuNR@SiO_2-MPTMS suspension (250 µL, 157 nM in 50 mM phosphate buffer pH 8) was mixed with DTNB solution (250 µL, 50 µM in 50 mM phosphate buffer pH 8), incubated in the dark for 90 min and centrifuged for 10 min at 9,000 rpm. The concentration of released TNB^{2-} in the supernatant was determined from a calibration curve obtained from standard solutions of cysteine between 5 and 200 µM, giving ε_{409nm} = 13450 $M^{-1}.cm^{-1}$.

2.4. Engineering solution-phase LSPR nanobiosensors

Bioconjugation of antibodies to AuNR@SiO_2 and AuNR@SiO_2-MPTMS/TEBA

Physisorption to AuNR@SiO_2: Goat anti-rIgG (15 µL, 1.2 mg/mL) was added to a suspension of AuNR@SiO_2 [AuNR@SiO_2]=15.7 pM, $OD_{\lambda max}$ ~ 0.6, ~ 1.5 mL in 5 mM phosphate buffer pH 7.4). The mixture was stirred for 90 min at room temperature and solid BSA was added to a final concentration of 0.5% (w/v) to block the non-specific adsorption sites and the suspension was kept under magnetic stirring for 45 min before the final washing step (see below).

Chemisorption to AuNR@SiO_2-MPTMS: TCEP solution (10 µL, 150 mM) was added to AuNR@SiO_2-MPTMS suspension ([AuNR@SiO_2] = 15.7 pM, $OD_{\lambda max}$ ~ 0.6, ~ 1.5 mL in 5 mM phosphate pH 7.4) in order to reduce any disulfide bridges that may have formed between the particles. After stirring for 90 min, particles were washed twice by centrifugation (10 min, 9000 rpm) and redispersed in phosphate buffer. Then, sulfo-MBS solution (20 µL, 3.75 mM) was added to the mixture. The suspension was stirred for 1 h before being purified twice by centrifugation (10 min, 9000 rpm) and redispersion in phosphate buffer. Finally, goat anti-rIgG solution (15 µL, 1.2 mg/mL) was added. After 90 min at room temperature, solid

BSA was added to a final concentration of 0.5% (w/v) to block the non-specific adsorption sites, and the suspension was stirred for 45 min before the final washing step (see below).

Chemisorption to AuNR@SiO_2-TEBA: Goat anti-rIgG solution 15 µL, 1.2 mg/mL) was added to a suspension of AuNR@SiO_2-TEBA ([AuNR@SiO_2] = 15.7 pM, $OD_{\lambda max}$ ~ 0.6, ~ 1.5 mL in 5 mM phosphate pH 7.4). Then $NaBH_3CN$ solution (20 µL, 75 mM) was added. The suspension was stirred for 17 h at room temperature. Then, solid BSA was added to a final concentration of 0.5% (w/v) to block the non-specific adsorption sites. The mixture was stirred for another 45 min before the final washing step (see below).

UV-visible spectra were recorded after each step and the three protocols described above were applied to (i) FITC-labeled goat anti-rIgG to quantify the amount of Ab per nanoparticle following our previously published procedure [34] (see supplementary data for the preparation of FITC-labeled goat anti-rIgG), and (ii) to affinity-purified goat anti-rabbit IgG (Ab) to prepare the nanoprobes.

Washing procedure: The particles were washed four times by centrifugation for 10 min at 9000 rpm. After each washing, supernatants S1 to S4 were collected and the pellets were redispersed in phosphate buffer containing BSA 0.25% w/v (1.5 mL). Supernatants S1 to S4 were centrifuged for another 15 min at 15,000 rpm in order to discard remaining particles which could interfere with the fluorescence measurements. Indirect quantification of FITC-labeled goat anti-rIgG grafted to AuNR@SiO_2 was performed from fluorescence measurements of S1 to S4 (supplementary data).

Evaluation of the performances of LSPR nanobiosensors in solution

Aliquots of rabbit IgG solution (4 µL, 2.5 mg/mL) were added to the three nanoprobe suspensions AuNR@SiO_2-Ab, AuNR@SiO_2-MPTMS-Ab and AuNR@SiO_2-TEBA-Ab (23.7 pM, $OD_{\lambda max}$ ~ 0.9, 400 µL) in plastic cuvettes, giving a final concentration between 25 and 1000 µg/mL. The mixtures were rapidly vortexed (~1 sec) after each addition. Extinction spectra were measured after one hour with a data interval of 0.3 nm.

3. Results and Discussion

Starting from core-shell AuNR@SiO_2 having an aspect ratio of 2.6 ± 0.2 and a silica shell thickness of 3.6 ± 0.2 nm, we elaborated three nanoprobes relying on three different surface chemistries: physisorption and, chemisorption via either thiol-terminated (MPTMS) or aldehyde-terminated (TEBA) silane condensation (Figure 1). In what follows, we first investigate the surface functionalization of AuNR@SiO_2 by silane condensation, related to the chemisorption strategy.

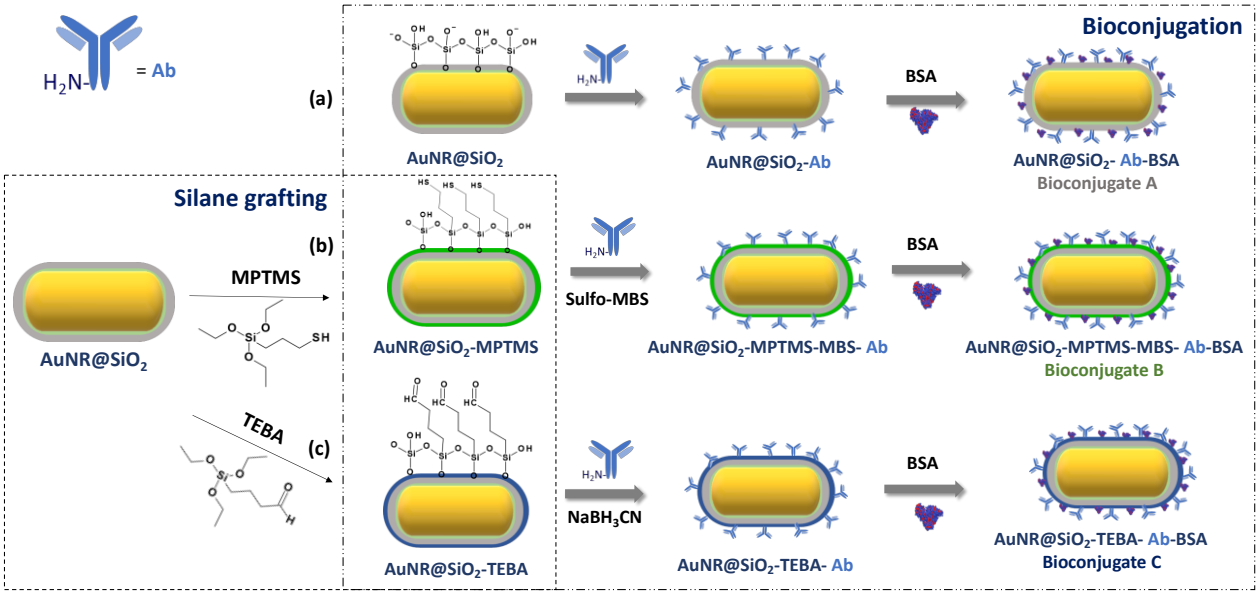

Figure 1. Sequences of reactions leading to AuNR@SiO_2-Ab bioconjugates A-C or nanoprobes A, B and C. Bioconjugation of goat anti-rabbit IgG antibody (Ab) to AuNR@SiO_2 by (a) physisorption and (b, c) chemisorption via MPTMS and TEBA condensation, respectively.

3.1. Surface functionalization of AuNR@SiO_2

In the chemisorption strategy, prior to conjugate the antibody to the nanoparticles, thiol or aldehyde functional groups were introduced at the surface of the silica shell through silanol condensation with alkoxysilanes MPTMS and TEBA, respectively. Nanoparticle suspensions were characterized by UV-Vis spectroscopy, DLS, ELS and TEM (Figure 2, Table 1). DLS is used in this work to evaluate the colloidal stability of the nanoparticles after grafting and not for size measurement (see experimental part for details), for which we rely on TEM images that provide more accurate data. Extinction spectra of AuNR@SiO_2 before and after silane condensation were normalized to visualize the displacement of the longitudinal plasmon band (l-LSPR) position and width. As shown in Figure 2a and Table 1, the l-LSPR band position is red-shifted by 12 nm and 4 nm after MPTMS and TEBA grafting, respectively. This shift is due to the change of the dielectric properties at the vicinity of the nanoparticles. The shift is larger for MPTMS, which might result from a larger density of MPTMS groups at the AuNR@SiO_2 surface. Moreover, asymmetric broadening of the l-LSPR band is noticed after silane condensation (Table 1, FWMH values) from 87 to 113 and 103 nm for MPTMS and TEBA, respectively. This broadening could be attributed to the coupling of plasmonic particles. No significant change in the hydrodynamic dimensions after alkoxysilane grafting was noticed from DLS measurements (Figure S 1c). One can however notice a moderate decrease in the relative intensity of the signal at ca. 13 nm associated to rotational diffusion for AuNR@SiO_2-MPTMS sample. The decrease in intensity of the peak associated to rotational diffusion, without a significant shift of the one associated to translational diffusion, could be assigned, based on the work of Liu et al. [32], to the formation of small (made of 3-4 NRs) aggregates for this sample (consistent with the significant broadening of its l-LSPR band), that will not compromise the colloidal stability of the nanoparticles.

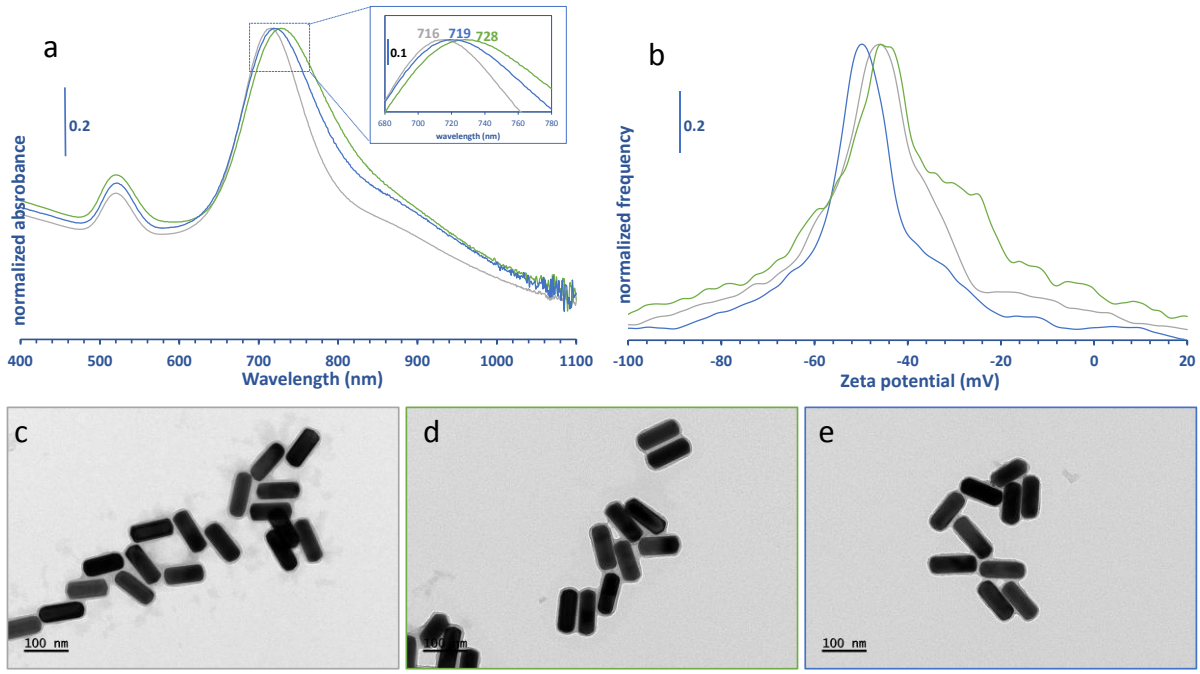

Figure 2. Characterization of AuNR@SiO_2 before (gray) and after silica shell functionalization by MPTMS (green) or TEBA (blue). (a) normalized extinction spectra, (b) zeta potential distribution at pH 8-9 and (c-e) representative TEM images.

Zeta potential measurements show a negative surface charge of the particles at pH 8-9 which ensures electrostatic repulsion between the particles. The zeta potential values are only slightly modified after silanes grafting (-49.1 vs -46.3 mV (MPTMS) and -44.3 mV (TEBA), Figure 2b, Table 1) reflecting the persistence of silanol groups after nanoparticle functionalization. Indeed, the evolution of the surface charge upon silane grafting depends on the surface coverage of silane and on the functional groups in the alkoxysilane molecule: for instance, Abadeer *et al.* [35] observed the neutralization of the surface after grafting of 3-azidopropyltrimethoxysilane while Kang *et al.* [36] found that the potential remains negative after chlorotrimethylsilane grafting whatever the pH. In the current case, the surface charge of particles decorated with sulfhydryl groups was slightly closer to the initial charge in comparison to the silica surface grafted with aldehyde groups. This could be explained by the fact that several silanols remain unbound to the silanes [26,37] and that the sulfhydryl group is ionizable (pK_a = 8-9) whereas the aldehyde group is neutral in the whole pH range.

TEM images of AuNRs@SiO_2 before and after silane condensation (Figure 2c-e) suggest a moderate increase of the silica shell thickness from 3.6 nm to about 4.5 nm (Table 1), in agreement with the literature [38]. This result is crucial since the LSPR immunosensor sensitivity depends on the silica shell thickness [21]. Furthermore, no formation of silica nanoparticles from homogeneous polycondensation of silanes was observed as shown on the TEM images of the as-synthesized samples before washing (Figure S 1a, b). This proves the selective and exclusive functionalization of the surface of AuNR@SiO_2 by silanes condensation on the silanol groups under the chosen conditions.

Table 1. Summary of AuNR@SiO_2 properties before and after silane condensation.

Sample	λ_{LSPR} (nm) / $\Delta\lambda$ (nm)	FWMH (nm)	Zeta potential (mV)	@SiO_2 (nm) (TEM)	@SiO_2 (nm) (XPS)
AuNR@SiO_2	716/ -	87	- 49 ± 1	3.6 ± 0.6	2.12
- MPTMS	728/12	113	- 46 ± 1	4.7 ± 1.2	4.21
- TEBA	720/4	103	- 44 ± 2	4.5 ± 0.9	2.53

XPS analysis was performed to evaluate the surface chemical composition of AuNR@SiO_2, AuNR@SiO_2-MPTMS and AuNR@SiO_2-TEBA, and highlight the grafting. Due to the large nanoparticles size compared to the XPS analysis depth (about 10 nm), it is possible to consider the analyzed samples as a bulk material (see supplementary data for detailed calculations). The survey XPS spectra (Figure S 2) show the presence of the same elements (O, S, C, and Si) on the particles surface before and after silanes grafting.

In order to discriminate the different chemical environments of sulfur, deconvolution of the S_{2p} peak was performed (Figure 3). Two contributions, with their main peaks at ~164.4 eV and ~163.0 eV assigned to thiol (-SH) and gold-bound sulfur (S-Au), respectively, were identified on the high resolution S_{2p} spectra for AuNR@SiO_2, AuNR@SiO_2-MPTMS, and AuNR@SiO_2-TEBA. The S-Au bonds are attributed to the interaction of MPTMS, used as primer, with AuNR surface. For the AuNR@SiO_2 sample, the thiol contribution – sulfur not bound to gold - (Figure 3a) could be assigned to MPTMS molecules self-condensed or co-condensed with TEOS and trapped into the silica shell [26,27]. The addition of MPTMS to AuNR@SiO_2 resulted in a clear increase of this contribution (Figure 3b) while it remained unchanged upon reaction with TEBA (Figure 3c). Besides these sulfur contributions, a third contribution at higher binding energy (~ 169.0 eV) assigned to oxidized sulfur forms (SO_4), was observed exclusively after silane condensation on the samples for both AuNR@SiO_2-MPTMS and AuNR@SiO_2-TEBA (Figure 3b). We first checked that this oxidized sulfur contribution did not originate from impurities in the silane samples and did not observe any oxidize sulfur on the S2p spectra recorded for MPTMS and no sulfur at all for TEBA (Figure S 3A). Another explanation could be the oxidation of free thiol that may occur in the presence of dissolved oxygen in the reaction medium [39]. To check whether this happened we applied the silane condensation conditions to bare AuNR@SiO_2 and measured the S2s and S2p peaks after heating in a EtOH/water mixture. The high resolution XPS spectra depicted in Figure S 3B clearly show the oxidation of sulfur during this process and unveil the origin of the oxidized sulfur observed above.

The XPS atomic ratios, calculated from the elemental analysis (Table S 1), further confirmed the grafting of MPTMS and TEBA owing to the significant increase in the Si/Au ratios and, for MPTMS, S/Au ratio. Note that, according to the Si/Au ratio, the amount of MPTMS appeared to be much larger than that of TEBA since it only increased from 0.97 to 1.08 in the latter case, versus 2.75 in the former case. All the same, S/Au ratio increased significantly upon MPTMS grafting (from 0.15 to 1.13, i.e. approx. 10 times higher) evidencing the presence of extra thiol groups and hence confirming the grafting of MPTMS.

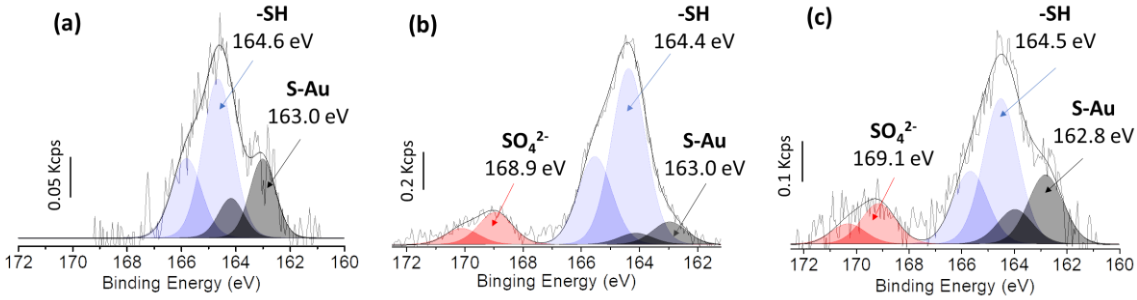

Figure 3. S_{2p} XPS spectra of AuNR@SiO_2 before (a) and after silane condensation with (b) MPTMS and (c) TEBA

XPS analysis does not distinguish between the surface-exposed and the trapped thiol functions inside the silica shell, induced by the primer used to grow the silica shell. Therefore, a colorimetric assay was used to quantify the free thiol groups at the surface of AuNR@SiO_2-MPTMS. The chemical quantification of thiol was carried out by Ellman's reagent as described in section 2.3. The average surface density estimated from the experimental measurements is 2.4 ± 0.6 SH/nm^2 (n=3) (Table S 2). Unfortunately, the aldehyde group density on the surface could not be measured by such assays.

3.2. Antibodies bioconjugation to core-shell nanoparticles

AuNR@SiO_2 were bioconjugated to goat rabbit anti-IgG antibody (anti-rIgG), according to two main approaches: physisorption to bare AuNR@SiO_2 and chemisorption to the functionalized AuNR@SiO_2-MPTMS and TEBA (Figure 1). Grafting of anti-rIgG by physisorption is based on the electrostatic interactions between the negatively charged surface of AuNR@SiO_2 and the basic amino acids of Ab (bioconjugate A). Chemisorption of anti-rIgG to AuNR@SiO_2-MPTMS was carried out using m-maleimidobenzoyl-N-hydroxysulfosuccinimide ester (sulfo-MBS) as coupling agent. The latter reacts with the free thiol function of MPTMS *via* its maleimide function to form stable thioether bond and with free primary amine functions of anti-rIgG *via* its N-hydroxysulfosuccinimide ester group to form amide bonds (Figure S 5; bioconjugate B). Chemisorption of anti-rIgG to AuNR@SiO_2-TEBA was performed by reductive amination between the aldehyde group of TEBA and the primary amine functions of anti-rIgG in the presence of sodium cyanoborohydride to reduce the intermediate Schiff base (Figure S 5; bioconjugate C). A blocking step to prevent non-specific adsorption was performed using bovine serum albumin (BSA) for all the bioconjugates.

The nanoparticles were analyzed after each synthesis step by UV-Visible spectroscopy as shown in Figure 4. All the bioconjugations were performed in triplicate and the position of the l-LSPR band (determined from the zero-crossing of the first order derivative using the 19-points method [31]) and its width are given in Table S 3 (mean and standard deviations calculated from three replicates). The l-LSPR band of AuNR@SiO_2, initially at 716.2 nm, red-shifted by 8.8 nm after addition of anti-rIgG, which proves its adsorption onto nanoparticles surface (Figure 4 a). Further red shift of 5.8 nm is noted after blocking step with BSA. The l-LSPR band of AuNR@SiO_2-MPTMS is progressively red-shifted by +3.0, +5.6 and +5 nm after reaction with sulfo-MBS, anti-rIgG grafting and blocking step with BSA,

respectively. Similar red-shifts of +2.5, +7.1 and +5.2 nm were observed for AuNR@SiO_2-TEBA following anti-rIgG grafting and BSA adsorption respectively. These results show that physisorption of antibody induces the largest shift of the l-LSPR band followed by chemisorption via TEBA and MPTMS, without significant increase of the FWHW.

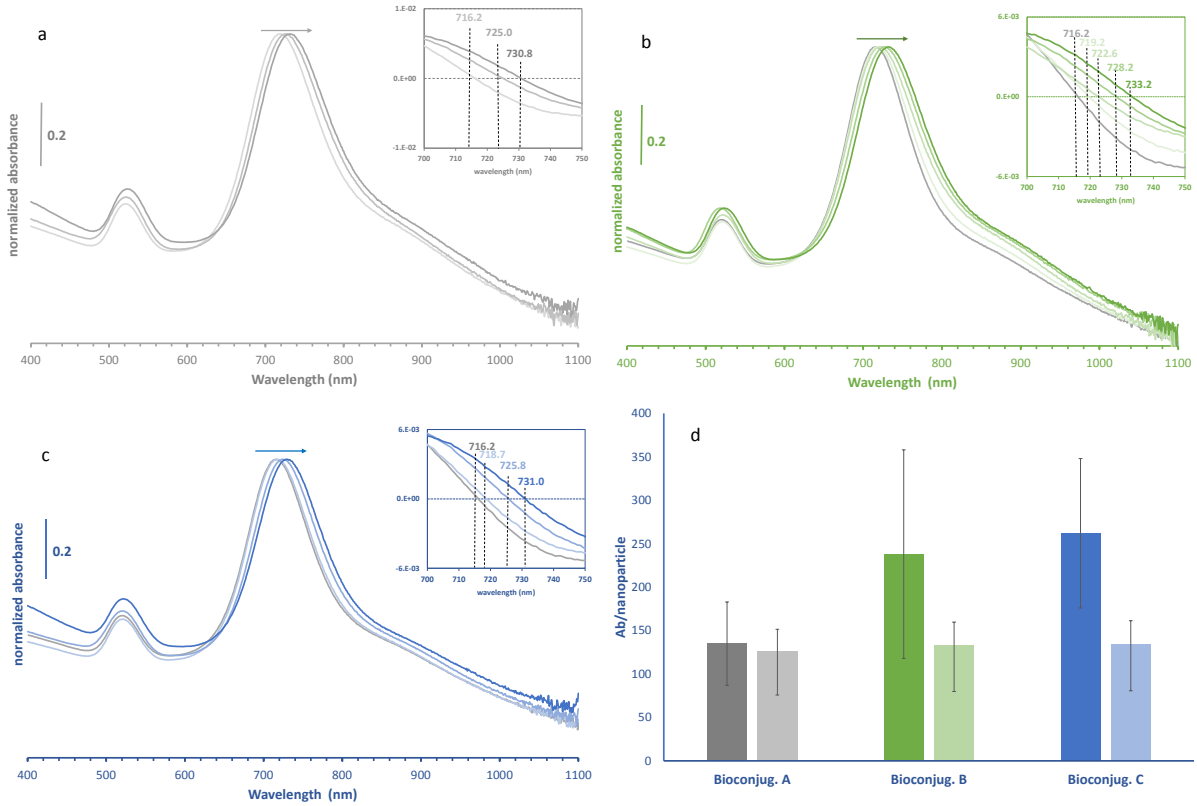

Figure 4. Normalized UV-visible spectra and their first derivatives (insets) recorded after the successive steps schematized in figure 1. (a) bioconjugate A (gray traces), (b) bioconjugate B (green traces), (c) bioconjugate C (blue traces); (d). Estimated (full bars) and theoretical (hatched bars) antibody surface coverage for bioconjugates 1, 2 and 3. Data are presented as mean ± SD (n =3).

DLS measurements in Figure S 6 (top) show an increase in the hydrodynamic diameter from about 110 nm to about 150 nm upon chemisorption of anti-rIgG to AuNR@SiO_2-MPTMS/TEBA while the size of the physisorption-based bioconjugate was unchanged. Figure S 6 (bottom) illustrates that bioconjugation increases the zeta potential from about -30/-27 mV to around -12/-16 mV in phosphate buffer. This result is expected as the nanoparticles surface charge should be close to that of the adsorbed protein [34]. These values are consistent with those previously measured for bioconjugated spherical gold [24] and Au@Ag core-shell [25] nanoparticles.

The amount of anti-rIgG grafted to the nanoparticles was indirectly estimated by measuring the concentration of the unreacted FITC-labeled anti-rIgG by spectrofluorimetry, as previously described [34] and detailed in the supplementary data section. The surface coverage expressed as anti-rIgG/nanoparticle ratio was estimated to 135 for AuNR@SiO_2-anti-rIgG (bioconjugate A), 238 for AuNR@SiO_2-MPTMS-anti-rIgG (bioconjugate B) and 262 for AuNR@SiO_2-TEBA-anti-rIgG (bioconjugate C) (Figure 4 d) on the basis of three

independent measurements. The theoretical antibody surface coverages estimated from the size of IgG (12x17x7 nm^3) and three possible orientations of the antibody molecules with respect to the nanoparticle surface [35] are also plotted in Figure 4d for comparison. The experimental surface coverage of bioconjugate A appeared to match the theoretical one. In contrast, the coverage values for bioconjugates B and C were about twice higher than the theoretical ones. It could be concluded from this result that the lower coverage of reactive functions in the case of AuNR@SiO_2-TEBA does not affect the amount of adsorbed anti-rIgG identical to that obtained for AuNR@SiO_2-MPTMS. The reason is probably because in the case of chemisorption, both strategies involve reaction with antibody amine groups, however, the number on anchoring points may affect the orientations of antibodies. The lower coverage obtained in the case of physisorption reflects the formation of a less dense antibody layer at the surface of the silica shell, that may also reflect a different orientation of the antibody molecules.

3.3. Evaluation of the LSPR nanobiosensors in solution

AuNR@SiO_2 bioconjugated to affinity-purified goat anti-rabbit IgG antibody (Ab), hereafter named nanoprobes A, B and C, were synthesized accordingly and used for the LSPR immunosensing of rabbit IgG in solution. Three nanoprobes were synthesized by the three surface chemistries described above: Ab physisorption for AuNR@SiO_2 (nanoprobe A) and Ab chemisorption for AuNR@SiO_2-MPTMS/TEBA (nanoprobes B and C, respectively). Transduction of the biorecognition is based on the l-LSPR band shift owing to RI change at proximity to the nanoparticles surface.

Response to rabbit IgG

A preliminary experiment was performed to assess the ability of the nanoprobes to sense the target antigen, namely rabbit IgG, via the shift of their l-LSPR band. The three nanoprobe suspensions were supplemented with 1000 ng/mL rIgG, the extinction spectrum of the mixtures was recorded at 10 min time interval and the shifts of the l-LSPR peak maximum (determined from the first derivative spectra, see below) were plotted as a function of time (Figure S 7). A progressive red shift of the l-LSPR band was observed until 40 min whose magnitude depended on the nanoprobe (A > B > C). This evidenced that the three nanoprobes were indeed able to optically detect the target in a short time scale. Interestingly, probes B and C provided the same response ($\Delta\lambda_{max}$) for 1000, 750 and 500 ng/mL rabbit IgG after 1 h incubation (Figure S 8, Table S 4) as a result of nanoprobe saturation from 500 ng /mL.

Next, the nanoprobe suspensions were supplemented with increasing concentrations of rabbit IgG ranging from 25 to 500 ng/mL and extinction spectra were recorded one hour after each new addition. The extinction spectra of nanoprobe A and their respective first and second derivatives are presented in Figure 5 (for nanoprobes B and C, see Figures S 9 and S 10, respectively).

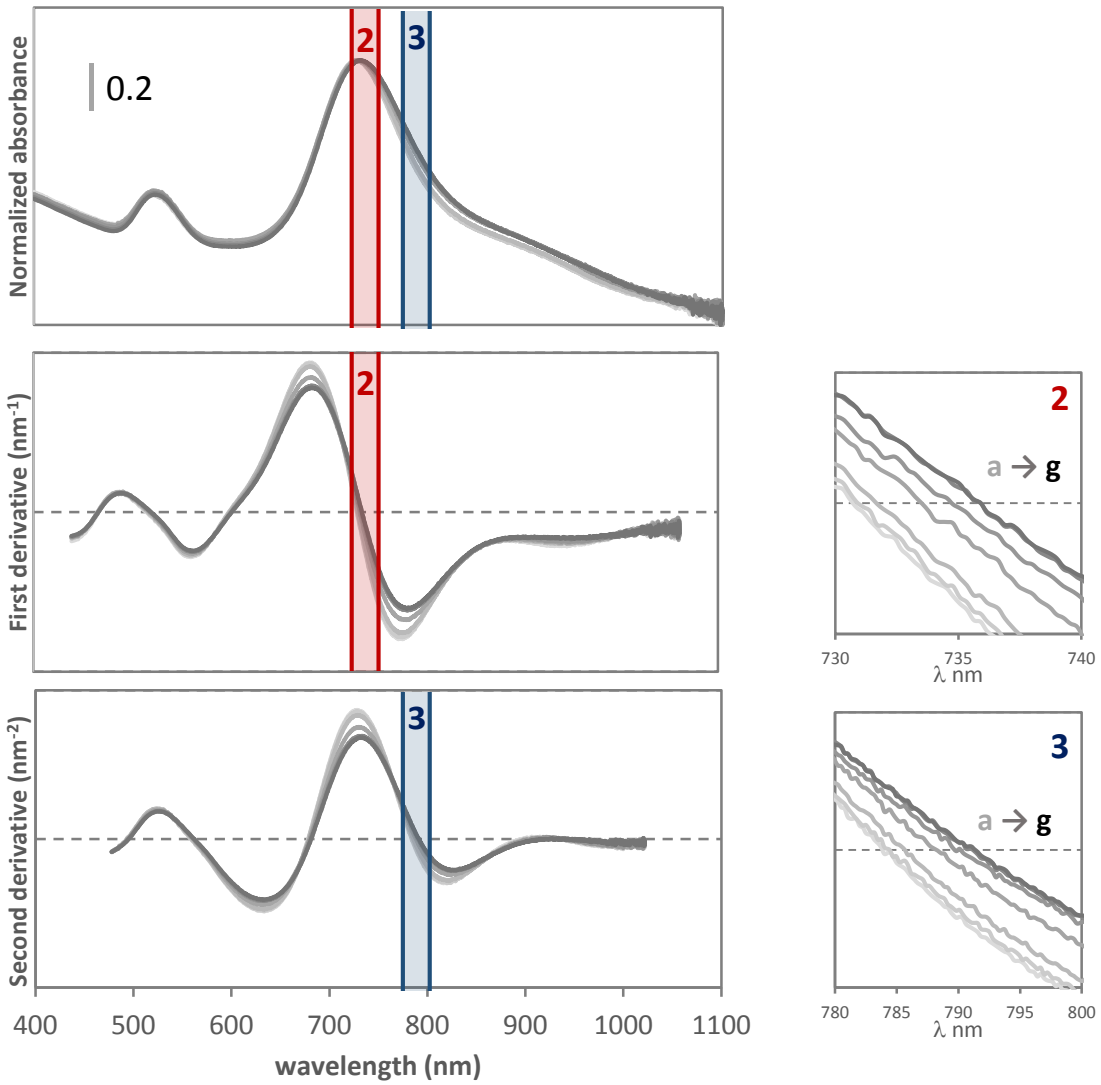

Figure 5. Normalized UV-visible spectra (top), first derivative (middle) and second derivative (bottom) a – g of nanoprobe A (physisorption) after exposure to different concentrations of rabbit IgG (0, 25, 50, 100, 150, 250 and 500 ng/mL). Inset: focus on the zero values of the first and second derivatives showing the l-LSPR band shifts at point 2 (λ_{max}) and point 3 (inflection point), respectively.

The maximum of the l-LSPR peak (Point 2) and the inflection point at the long wavelength side (Point 3) are defined by dotted lines. Point 2 is obtained from the 0 value of the first order derivative spectrum while Point 3 is obtained from the 0 value of the second order derivative spectrum. A progressive shift of the plasmon band is observed subsequently to the addition of increasing amounts of rabbit IgG for all the nanoprobes. The corresponding values of the tracking points 2 and 3 are summarized in Table 2. Displacements of up to 4.9, 4.2 and 2.4 nm were determined from point 2 and 7.6, 9.3 and 3.0 nm were determined from point 3 for AuNR@SiO_2-Ab (nanoprobe A), AuNR@SiO_2-MPTMS-Ab (nanoprobe B) and AuNR@SiO_2-TEBA-Ab (nanoprobe C), respectively. Note that these displacements are smaller than those recorded after antibodies adsorption during bioconjugate engineering, possibly because the distance to the plasmonic surfaces are bigger.

Table 2. Summary of l-LSPR band shifts ($\Delta\lambda_{LSPR}$) for nanoprobes A, B and C as a function of rabbit IgG concentration according to points 2 and 3; the shift of the l-LSPR band after addition of mouse IgG (mIgG) is also reported to ascertain the specificity of the nanoprobes. Data are given as mean ± SD (n=2)

		[rIgG][a] (ng/mL)							[mIgG][b] (ng/mL)	
		0	25	50	100	150	250	500	1000	2000
Nanoprobe A	Pt 2	0.03[c]	0.3 ± 0.2	0.9 ± 0.7	2.6 ± 0.4	3.8 ± 0.9	4.9 ± 0.2	4.9 ± 0.2	0.09	0.17
	Pt 3	0.45	0.7 ± 0.2	2.3 ± 0.7	4.6 ± 0.4	6.5 ± 0.9	7.4 ± 0.2	7.6 ± 0.2	0.66	0.33
Nanoprobe B	Pt 2	0.08	0.30 ± 0.03	0.50 ± 0.05	1.7 ± 0.1	2.7 ± 0.1	3.7 ± 0.2	4.2 ± 0.2	-0.25	-0.06
	Pt 3	0.46	2.4 ± 0.2	2.8 ± 0.3	4.8 ± 0.2	6.5 ± 0.3	8.5 ± 0.4	9.3 ± 0.5	1.72	0.84
Nanoprobe C	Pt 2	0.02	0.10 ± 0.01	0.6 ± 0.1	1.8 ± 0.2	2.4 ± 0.2	2.5 ± 0.2	2.4 ± 0.2	0.025	0.03
	Pt 3	0.24	0.05	1.0 ± 0.1	2.2 ± 0.2	2.7 ± 0.3	3.2 ± 0.3	3.1 ± 0.3	0.34	0.35

[a] specific recognition; [b] nonspecific protein; [c] standard deviation of the blank samples

Larger shifts are observed from point 3 because it takes into account both the position of the LSPR peak maximum and its broadening [31]. Band broadening could be due to nanoparticles cross-linking *via* rabbit IgG, nevertheless no color change is noticed for the colloidal solutions. The specificity of the nanoprobes was also checked by adding mouse IgG instead of rabbit IgG at two concentrations (1 and 2 µg/mL, values in Table 2, spectra in Figure S 12). The three nanoprobes gave shifts that did not significantly differ from those of the blanks. This proves the specificity of the nanoprobes for rabbit IgG detection.

Stability and analytical performances

DLS measurements (Figure S 11) show that nanoprobes maintain a good colloidal stability after rabbit IgG capture. This result dramatically differs from previous works dealing with solution-phase AuNR-based LSPR biosensors for which addition of target resulted in nanoparticles aggregation that translated into large redshifts and drastic reduction of plasmon band intensity [15–17]. The l-LSPR band shifts ($\Delta\lambda_{LSPR}$) measured at points 2 and 3 were plotted as a function of rabbit IgG concentration (Figure 6). Non-linear regression of the data was performed according to the 4-parameter logistic equation as detailed in supplementary data section. The analytical performances of the three nanoprobes (IC_{50}, dynamic range and limit of detection (LoD)) as well as the parameters attesting the accuracy of the model (R^2, χ^2) are summarized in Table 3. The LoD is defined as the concentration corresponding to 10 % of the maximum response (IC_{10}) [40].

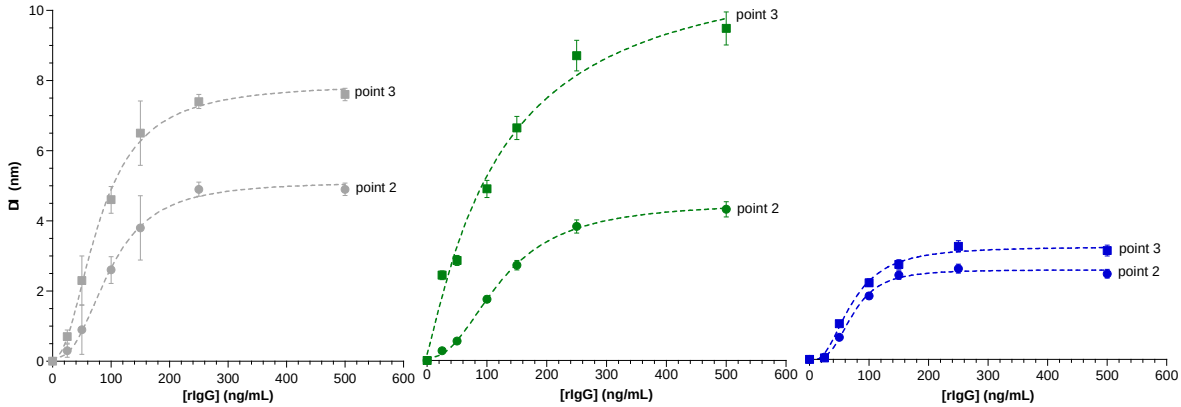

Figure 6. LSPR nanobiosensors dose-response curves obtained by plotting point 2 (squares) or point 3 (dots) vs. rabbit IgG concentration for nanoprobe A (left), nanoprobe B (middle) and nanoprobe C (right). Data are presented as mean ± SD (n =2). Curves result from non-linear fitting of data according to 4-parameter logistic equation.

The dose-response curves show similar trends for nanoprobes A and B and clearly lower performances for nanoprobe C. In all cases, monitoring the wavelength of the second derivative inflection point gave a larger response that following the maximum of l-LSPR position. The LoD were estimated to 27 ng/mL, 12 ng/mL and 31 ng/mL (80 – 207 pM) for nanoprobes A, B and C respectively (point 3). The LoD of nanoprobes A and B were about 3 to 4-fold lower than those measured with closely related systems for the detection of human IgG (0.4 nM) [16], which proves their excellent analytical performances.

Table 3. Analytical performances and fitting parameters for LSPR nanobiosensing of rabbit IgG with nanoprobes A, B and C

	Nanoprobe A		Nanoprobe B		Nanoprobe C	
	point 2	point 3	point 2	point 3	point 2	point 3
$\Delta\lambda_{max}$	5.1 ± 0.2	7.9 ± 0.3	4.4 ± 0.1	12 ± 2	2.51 ± 0.07	3.2 ± 0.1
IC_{50} (ng/mL)	98 ± 6	80 ± 6	125 ± 5	120 ± 50	73 ± 4	70 ± 6
χ^2	0.082	0.200	0.019	1.05	0.029	0.065
R^2	0.997	0.997	0.999	0.985	0.996	0.994
LoD (ng/mL)[a]	38	27	43	12	36	31
DR (ng/mL)[b]	54 - 156	40 - 140	64 - 207	26 - 206	46 - 105	41 - 117

[a] calculated from 10% of $\Delta\lambda_{max}$; [b] dynamic range (DR) corresponding to concentrations giving from 20 to 80% of $\Delta\lambda_{max}$

Altogether, the three LSPR nanobiosensors had excellent analytical performances with narrow dynamic ranges and the lowest LoD equal to 12 ng/mL. The best analytical performances are provided by nanoprobe B, built on AuNR@SiO_2-MPTMS surface, in terms of LoD, IC_{50}, and dynamic range. This chemisorption strategy that induced a high coverage of reactive functions, obviously led to efficient nanoprobes with accessible and well-oriented antibodies. Nanoprobe A, that was built by physisorption of anti-rIgG also exhibits remarkable performances, close to those of nanoprobe B. These nice results for "a simple physisorption strategy" are probably the fruit of the silica layer and its highly negative charge that leads to strong electrostatic interactions. Beside these electrostatic interactions, silanol

groups, present with high density (~5 Si-OH/nm²) are easily involved in H bonds with amine groups [26]. They certainly provide cooperative interactions upon anti-rIgG physisorption further stabilizing the bioconjugate. In addition, for an LSPR biosensor to be efficient, binding of analyte should occur within the sensing volume that is determined by the decay length. In the case of nanoprobe A, the bioreceptor is the closest to the gold surface which gives rise to larger LSPR peak shifts and further improves its performances. Nanoprobe C gave much lower responses and a comparatively narrower dynamic range than nanoprobes A and B, possibly because of an unfavorable orientation of the capture antibody that hinders proper antigen binding or a limited accessibility of the bioreceptors. The low coverage of silanes during the preparation of AuNR@SiO_2-TEBA may be one of the reasons to these lower performances even if electrostatic interactions should have compensated the reactivity. Nevertheless, the difference observed between nanoprobes B and C, despite identical amounts of bioreceptors on their surface, clearly highlights the importance of the surface chemistry on bioreceptor orientation and nanoprobes efficiency for biosensing.

4. Conclusion and perspectives

We have reported here an in-depth investigation of the biofunctionalization of gold nanorods coated with an ultrathin layer of silica (AuNR@SiO_2) to elaborate LSPR nanobiosensors for solution-phase biosensing of proteins. Three surface chemistries were explored to attach the capture antibody at the surface of AuNR@SiO_2, the first *via* physisorption to the negatively charged silica-coated nanorods and the second and third by first condensing reactive silane terminated by thiol (MPTMPS) or aldehyde (TEBA) to the silica layer, then cross-reacting with the antibodies amino-groups to achieve a stable chemisorption. Each step of surface functionalization was characterized with DLS, electron microscopy, zetametry, XPS and UV-Visible spectroscopy. Silane grafting was achieved with higher rate in the case of MPTMS than for TEBA, but the colloidal stability was preserved for both routes. The coverage rate of immobilized antibodies was estimated by fluorimetric analysis of the supernatants and was twice lower for the physisorption bioconjugate while identical for the two chemisorbed bioconjugates despite the differences in silane coverage. The resulting nanoprobes were efficient for the detection of the target analyte; the LSPR peak of the three nanoprobes shifted to the red and the shifts were related to the concentration between 25 and 500 ng/mL. These shifts could be readily measured with a benchtop UV-Visible spectrometer without the need of a separation step. The three probes were also highly specific since no shift was observed for an unrelated analyte. The nanobiosensors maintain an excellent colloidal stability after analyte recognition and their analytical performances were extremely high with an LoD down to 12 ng/mL in the case of the chemisorbed antibodies on MPTMS-modified AuNR@SiO_2. As a perspective, the LSPR response could be further optimized by choosing AuNR whose dimensions determine a decay length that matches the thickness of the bioreceptor – analyte couple. Another perspective of signal improvement could be the reduction of the bioreceptor size (that is the thickness of the bioreceptor layer) to maximize the occupation of the sensing volume.

Acknowledgement

This work was financially supported by the French National Research Agency (Project No. ANR-16-CE07-0031-01) and by IMat, L'Institut de Science des Matériaux de l'Alliance Sorbonne Université, France

Authors contribution

Conceptualization & Methodology: SB & MS; Investigation: VP, JB, AM, CM, SMC; Writing - Original Draft: FS; Writing - Review & Editing: SB & MS; Supervision: SB, MS, JB; Funding acquisition: SB.

Appendix A. Supplementary data

Supplementary Figures:

Figure S 1. TEM images of AuNR@SiO_2 silanized with (a) MPTMS and (b) TEBA before washing step (c) Hydrodynamic diameter of silanized AuNR@SiO_2 samples after washing

Figure S 2. Survey XPS spectra of AuNR@SiO_2 before (black) and after reaction of MPTMS (red) and TEBA (blue).

Figure S 3. XPS investigation of the origin of oxidized sulfur in the functionalized $AuNR@SiO_2$. Panel A shows S2p spectra for the reagents silanes, MPTMS and TEBA, the latter contains no sulfur and Panel B shows the S2s and S2p spectra for $AuNR@SiO_2$ before and after thermal treatment in EtOH/H2O mixture without adding any silane, this treatment clearly affects the oxidation state of sulfur and new species at higher binding energy appear on S2p peak

Figure S 4. UV-Vis spectra of DTNB (green) and supernatants of silanized (red) and non-silanized (black) AuNR@SiO2 samples after reaction with DTNB.

Figure S 5. General scheme for grafting of anti-rabbit IgG to AuNR@SiO2 via (a) surface thiol functions and (b) surface aldehyde functions

Figure S 6. DLS (top) and zeta potential measurements (bottom) of AuNR@SiO_2(-MPTMS/TEBA) before and after bioconjugation and non-specific blocking step with BSA at pH 7.4.

Figure S 7. Shift of the l-LSPR peak position over time for AuNR@SiO2-Ab (nanoprobe A), AuNR@SiO2-MPTMS-Ab (nanoprobe B), and AuNR@SiO2-TEBA-Ab (nanoprobe C) in the presence of rabbit IgG antigen (1 µg/mL)

Figure S 8. Normalized extinction spectra (top) and their first derivatives (bottom) of nanoprobes after addition of rabbit IgG in the range 500-1000 ng/mL. AuNR@SiO_2-Ab (nanoprobe 1, gray traces). (B) AuNR@SiO_2-MPTMS-Ab (nanoprobe B, green traces) and (C) AuNR@SiO_2-TEBA- Ab (nanoprobe C, blue traces)

Figure S 9. Normalized UV-visible spectra (top), first derivative (middle) and second derivative (bottom) of AuNR@SiO_2-MPTMS-Ab (nanoprobe B) after exposure to different rabbit IgG concentrations (0, 25, 50, 100, 150, 250 and 500 ng/mL)

Figure S 10. Normalized UV-visible spectra (top), first derivative (middle) and second derivative (bottom) of AuNR@SiO_2-TEBA-Ab (nanoprobe C) after exposure to different rabbit IgG concentrations (0, 25, 50, 100, 150, 250 and 500 ng/mL)

Figure S 11. DLS measurements before and after addition of rabbit IgG for (a) AuNR@SiO_2-Ab (nanoprobe A), (b) AuNR@SiO_2-MPTMS-Ab (nanoprobe B) and (c) AuNR@SiO_2-TEBA-Ab (nanoprobe C)

Figure S 12. Normalized UV-visible spectra (left), first derivative (middle) and second derivative (right) of the nanoprobes after exposure to solutions of non-specific mouse IgG (0, 1 or 2 µg/mL); (a) AuNR@SiO2-Ab (nanoprobe A) (b) AuNR@SiO2-MPTMS-Ab (nanoprobe B) and (c) AuNR@SiO2-TEBA-Ab (nanoprobe C)

Supplementary Tables:

Table S 1. XPS atomic ratios of chemical elements for bare and silanized AuNR@SiO_2

Table S 2. Assay of surface thiols by DTNB on three batches of AuNR@SiO2 silanized by MPTMS

Table S 3. Summary of l-LSPR band positions and FWMH for conjugated AuNR@SiO_2-Ab (bioconjugate 1), AuNR@SiO_2-MPTMS-Ab (bioconjugate 2), AuNR@SiO_2-TEBA-Ab (bioconjugate 3). Data are presented as mean ± SD (n =3)

Table S 4. Shifts of l-LSPR peak maximum of nanoprobes A, B and C upon addition of rIgG solution (500 – 1000 ng/mL)

References

[1] M.-C. Estevez, M.A. Otte, B. Sepulveda, L.M. Lechuga, Trends and challenges of refractometric nanoplasmonic biosensors: A review, Anal. Chim. Acta. 806 (2014) 55–73. https://doi.org/10.1016/j.aca.2013.10.048.

[2] B. Sepúlveda, P.C. Angelomé, L.M. Lechuga, L.M. Liz-Marzán, LSPR-based nanobiosensors, Nano Today. 4 (2009) 244–251. https://doi.org/10.1016/j.nantod.2009.04.001.

[3] M. Soler, C.S. Huertas, L.M. Lechuga, Label-free plasmonic biosensors for point-of-care diagnostics: a review, Expert Rev. Mol. Diagn. 19 (2019) 71–81. https://doi.org/10.1080/14737159.2019.1554435.

[4] H. Chen, L. Shao, Q. Li, J. Wang, Gold nanorods and their plasmonic properties, Chem Soc Rev. 42 (2013) 2679–2724. https://doi.org/10.1039/C2CS35367A.

[5] G.J. Nusz, A.C. Curry, S.M. Marinakos, A. Wax, A. Chilkoti, Rational Selection of Gold Nanorod Geometry for Label-Free Plasmonic Biosensors, ACS Nano. 3 (2009) 795–806. https://doi.org/10.1021/nn8006465.

[6] L. Tian, E. Chen, N. Gandra, A. Abbas, S. Singamaneni, Gold Nanorods as Plasmonic Nanotransducers: Distance-Dependent Refractive Index Sensitivity, Langmuir. 28 (2012) 17435–17442. https://doi.org/10.1021/la3034534.

[7] K.M. Mayer, J.H. Hafner, Localized Surface Plasmon Resonance Sensors, Chem. Rev. 111 (2011) 3828–3857. https://doi.org/10.1021/cr100313v.

[8] C.J. Murphy, T.K. Sau, A.M. Gole, C.J. Orendorff, J. Gao, L. Gou, S.E. Hunyadi, T. Li, Anisotropic Metal Nanoparticles: Synthesis, Assembly, and Optical Applications, J. Phys. Chem. B. 109 (2005) 13857–13870. https://doi.org/10.1021/jp0516846.

[9] H.-H. Chang, C.J. Murphy, Mini Gold Nanorods with Tunable Plasmonic Peaks beyond 1000 nm, Chem. Mater. 30 (2018) 1427–1435. https://doi.org/10.1021/acs.chemmater.7b05310.

[10] C.-D. Chen, S.-F. Cheng, L.-K. Chau, C.R.C. Wang, Sensing capability of the localized surface plasmon resonance of gold nanorods, Biosens. Bioelectron. 22 (2007) 926–932. https://doi.org/10.1016/j.bios.2006.03.021.

[11] V. Pellas, D. Hu, Y. Mazouzi, Y. Mimoun, J. Blanchard, C. Guibert, M. Salmain, S. Boujday, Gold Nanorods for LSPR Biosensing: Synthesis, Coating by Silica, and Bioanalytical Applications, Biosensors. 10 (2020) 146. https://doi.org/10.3390/bios10100146.

[12] S.M. Marinakos, S. Chen, A. Chilkoti, Plasmonic Detection of a Model Analyte in Serum by a Gold Nanorod Sensor, Anal. Chem. 79 (2007) 5278–5283. https://doi.org/10.1021/ac0706527.

[13] K.M. Mayer, S. Lee, H. Liao, B.C. Rostro, A. Fuentes, P.T. Scully, C.L. Nehl, J.H. Hafner, A Label-Free Immunoassay Based Upon Localized Surface Plasmon Resonance of Gold Nanorods, ACS Nano. 2 (2008) 687–692. https://doi.org/10.1021/nn7003734.

[14] C. Yu, J. Irudayaraj, Multiplex Biosensor Using Gold Nanorods, Anal. Chem. 79 (2007) 572–579. https://doi.org/10.1021/ac061730d.

[15] Z.R. Guo, C.R. Gu, X. Fan, Z.P. Bian, H.F. Wu, D. Yang, N. Gu, J.N. Zhang, Fabrication of Anti-human Cardiac Troponin I Immunogold Nanorods for Sensing Acute Myocardial Damage, Nanoscale Res. Lett. 4 (2009) 1428–1433. https://doi.org/10.1007/s11671-009-9415-6.

[16] C. Wang, Y. Chen, T. Wang, Z. Ma, Z. Su, Biorecognition-Driven Self-Assembly of Gold Nanorods: A Rapid and Sensitive Approach toward Antibody Sensing, Chem. Mater. 19 (2007) 5809–5811. https://doi.org/10.1021/cm0700899.

[17] C. Wang, J. Irudayaraj, Gold Nanorod Probes for the Detection of Multiple Pathogens, Small. 4 (2008) 2204–2208. https://doi.org/10.1002/smll.200800309.

[18] S. Centi, F. Ratto, F. Tatini, S. Lai, R. Pini, Ready-to-use protein G-conjugated gold nanorods for biosensing and biomedical applications, J. Nanobiotechnology. 16 (2018). https://doi.org/10.1186/s12951-017-0329-7.

[19] S. Lai, S. Centi, C. Borri, F. Ratto, L. Cavigli, F. Micheletti, B. Kemper, S. Ketelhut, T. Kozyreva, L. Gonnelli, F. Rossi, S. Colagrande, R. Pini, A multifunctional organosilica cross-linker for the bio-conjugation of gold nanorods, Colloids Surf. B Biointerfaces. 157 (2017) 174–181. https://doi.org/10.1016/j.colsurfb.2017.05.068.

[20] C. Wu, Q.-H. Xu, Stable and Functionable Mesoporous Silica-Coated Gold Nanorods as Sensitive Localized Surface Plasmon Resonance (LSPR) Nanosensors, Langmuir. 25 (2009) 9441–9446. https://doi.org/10.1021/la900646n.

[21] L. Song, L. Zhang, Y. Huang, L. Chen, G. Zhang, Z. Shen, J. Zhang, Z. Xiao, T. Chen, Amplifying the signal of localized surface plasmon resonance sensing for the sensitive detection of Escherichia coli O157:H7, Sci. Rep. 7 (2017) 3288. https://doi.org/10.1038/s41598-017-03495-1.

[22] V. Pellas, J. Blanchard, C. Guibert, J.-M. Krafft, A. Miche, M. Salmain, S. Boujday, Gold Nanorod Coating with Silica Shells Having Controlled Thickness and Oriented Porosity: Tailoring the Shells for Biosensing, ACS Appl. Nano Mater. 4 (2021) 9842–9854. https://doi.org/10.1021/acsanm.1c02297.

[23] C. Wang, Z. Ma, T. Wang, Z. Su, Synthesis, Assembly, and Biofunctionalization of Silica-Coated Gold Nanorods for Colorimetric Biosensing, Adv. Funct. Mater. 16 (2006) 1673–1678. https://doi.org/10.1002/adfm.200500898.

[24] M. Ben Haddada, D. Hu, M. Salmain, L. Zhang, C. Peng, Y. Wang, B. Liedberg, S. Boujday, Gold nanoparticle-based localized surface plasmon immunosensor for staphylococcal enterotoxin A (SEA) detection, Anal. Bioanal. Chem. 409 (2017) 6227–6234. https://doi.org/10.1007/s00216-017-0563-8.

[25] A. Loiseau, L. Zhang, D. Hu, M. Salmain, Y. Mazouzi, R. Flack, B. Liedberg, S. Boujday, Core-Shell Gold/Silver Nanoparticles for Localized Surface Plasmon Resonance-Based Naked-Eye Toxin Biosensing, ACS Appl. Mater. Interfaces. 11 (2019) 46462–46471. https://doi.org/10.1021/acsami.9b14980.

[26] N. Aissaoui, L. Bergaoui, J. Landoulsi, J.-F. Lambert, S. Boujday, Silane Layers on Silicon Surfaces: Mechanism of Interaction, Stability, and Influence on Protein Adsorption, Langmuir. 28 (2012) 656–665. https://doi.org/10.1021/la2036778.

[27] S. Boujday, J.-F. Lambert, M. Che, Amorphous Silica as a Versatile Supermolecular Ligand for NiII Amine Complexes: Toward Interfacial Molecular Recognition, ChemPhysChem. 5 (2004) 1003–1013. https://doi.org/10.1002/cphc.200400008.

[28] T. Hendel, M. Wuithschick, F. Kettemann, A. Birnbaum, K. Rademann, J. Polte, In Situ Determination of Colloidal Gold Concentrations with UV–Vis Spectroscopy: Limitations and Perspectives, ACS Anal. Chem. 86 (2014) 11115–11124. https://doi.org/10.1021/ac502053s.

[29] L. Scarabelli, M. Grzelczak, L.M. Liz-Marzán, Tuning Gold Nanorod Synthesis through Prereduction with Salicylic Acid, ACS Chem. Mater. 25 (2013) 4232–4238. https://doi.org/10.1021/cm402177b.

[30] P. Chen, B. Liedberg, Curvature of the Localized Surface Plasmon Resonance Peak, Anal. Chem. 86 (2014) 7399–7405. https://doi.org/10.1021/ac500883x.

[31] P. Chen, N.T. Tran, X. Wen, Q. Xiong, B. Liedberg, Inflection Point of the Localized Surface Plasmon Resonance Peak: A General Method to Improve the Sensitivity, ACS Sens. 2 (2017) 235–242. https://doi.org/10.1021/acssensors.6b00633.

[32] H. Liu, N. Pierre-Pierre, Q. Huo, Dynamic light scattering for gold nanorod size characterization and study of nanorod–protein interactions, Gold Bull. 45 (2012) 187–195. https://doi.org/10.1007/s13404-012-0067-4.

[33] J.H. Al Mahrooqi, E.A. Mun, A.C. Williams, V.V. Khutoryanskiy, Controlling the Size of Thiolated Organosilica Nanoparticles, Langmuir. 34 (2018) 8347–8354. https://doi.org/10.1021/acs.langmuir.8b01556.

[34] L. Zhang, D. Hu, M. Salmain, B. Liedberg, S. Boujday, Direct quantification of surface coverage of antibody in IgG-Gold nanoparticles conjugates, Talanta. 204 (2019) 875–881. https://doi.org/10.1016/j.talanta.2019.05.104.

[35] N.S. Abadeer, M.R. Brennan, W.L. Wilson, C.J. Murphy, Distance and Plasmon Wavelength Dependent Fluorescence of Molecules Bound to Silica-Coated Gold Nanorods, ACS Nano. 8 (2014) 8392–8406. https://doi.org/10.1021/nn502887j.

[36] H. Kang, C. Haynes, Interactions between Silica-Coated Gold Nanorod Substrates and Hydrophobic Analytes in Colloidal Surface-Enhanced Raman Spectroscopy, J. Phys. Chem. C. 123 (2019) 24685–24697. https://doi.org/10.1021/acs.jpcc.9b06044.

[37] M. Ben Haddada, J. Blanchard, S. Casale, J.-M. Krafft, A. Vallée, C. Méthivier, S. Boujday, Optimizing the immobilization of gold nanoparticles on functionalized silicon surfaces: amine- vs thiol-terminated silane, Gold Bull. 46 (2013) 335–341. https://doi.org/10.1007/s13404-013-0120-y.

[38] T. Inose, T. Oikawa, M. Tokunaga, N. Yamauchi, K. Nakashima, C. Kato, K. Hatoyama, T. Kamei, K. Gonda, Y. Kobayashi, Development of composite nanoparticles composed of silica-coated nanorods and single nanometer-sized gold particles toward a novel X-ray contrast agent, Mater. Sci. Eng. B. 262 (2020) 114716. https://doi.org/10.1016/j.mseb.2020.114716.

[39] G.A. Bagiyan, I.K. Koroleva, N.V. Soroka, A.V. Ufimtsev, Oxidation of thiol compounds by molecular oxygen in aqueous solutions, Russ. Chem. Bull. 52 (2003) 1135–1141. https://doi.org/10.1023/A:1024761324710.

[40] J.C. Soares, A.C. Soares, P.A.R. Pereira, V. da C. Rodrigues, F.M. Shimizu, M.E. Melendez, C.S. Neto, A.L. Carvalho, F.L. Leite, S.A.S. Machado, O.N. Oliveira, Adsorption according to the Langmuir–Freundlich model is the detection mechanism of the antigen p53 for early diagnosis of cancer, Phys. Chem. Chem. Phys. 18 (2016) 8412–8418. https://doi.org/10.1039/C5CP07121F.